42nd AIAA Aerospace Sciences Meeting and Exhibit
5 - 8 January 2004, Reno, Nevada

AIAA 2004-256

AIAA 2004-0256
Receptivity to Freestream Disturbances of a Mach 10 Nonequilibrium Reacting Oxygen Flow over A Flat Plate

Yanbao Ma and Xiaolin Zhong
University of California, Los Angeles

42th Aerospace Sciences Meeting & Exhibit
January 5–8, 2004 / Reno, NV

Linear Stability and Receptivity to Frees-Stream Disturbances of a Mach 10 Nonequilibrium Reacting Oxygen Flow over A Flat Plate

Yanbao Ma*and Xiaolin Zhong†
University of California, Los Angeles, California 90095

Abstract

In this paper, we continue to study receptivity mechanisms of hypersonic boundary layers to freestream disturbances by using both linear stability theory (LST) and direct numerical simulations (DNS). A high-order shock fitting scheme is used in the numerical simulations in order to account for the effects of interactions between freestream disturbance waves and the oblique shock wave. Beside of perfect flow, a computational code is developed for numerical simulation of transient hypersonic nonequilibrium flow by combining a fifth-order shock-fitting scheme with additive semi-implicit Runge-Kutta (SIRK) methods. Meanwhile, a LST code based on multi-domain spectral method is developed to study the boundary-layer stability characteristics relevant to the receptivity study. Before applying these codes in receptivity studies, extensive testings and evaluations have been conducted to ensure that correct and accurate results of both the numerical simulations and the linear stability analysis. After code validation, receptivities of hypersonic boundary-layers of a Mach 10.0 oxygen flow over a flat plate to freestream disturbances are studied. The linear stability characteristics of the boundary-layer wave modes and their mutual resonant interactions are studied by both LST and DNS. Then, two types of freestream disturbances,i.e, fast acoustic waves, slow acoustic waves, are introduced in front of the oblique shock to investigate how freestream disturbances interact with the shock, penetrate the boundary layer and ultimately induce boundary-layer disturbances. The effects of incident wave angles, forcing wave frequencies, and wall temperature perturbation conditions on the receptivity are studied. For Mach 10.0 oxygen flow, receptivities are studied in both perfect gas and thermochemically nonequilibrium regime to investigate the real gas effects on the receptivity and stability of hypersonic boundary-layer flow. It is found that, in addition to the conventional first and second Mack modes, there exist a family of stable wave modes in the supersonic boundary layer. These modes play a very important role in the receptivity process of excitation of the unstable Mack modes, especially the second mode. These stable modes are termed mode I, mode II, etc. Though mode I and mode II waves are linearly stable, they can have resonant (synchronization) interactions with both acoustic waves and the Mack-mode waves. For different flow conditions, the results show that the forcing fast acoustic waves do not interact directly with the unstable Mack modes. Instead, the stable mode I waves play an important role in the receptivity process because they interact with both the forcing acoustic waves and the unstable Mack-mode waves. Through the interactions, the stable mode I waves transfer wave energy from the forcing fast acoustic waves to the second Mack-mode waves. In receptivity to freestream slow acoustic waves, Mack mode waves are generated near the leading edge due to resonant interactions between slow acoustic waves and the first-mode waves. Because mode I are more stable than the first mode, the receptivity to freestream slow acoustic waves with low incident angle are much stronger than that to freestream fast acoustic waves at the same angle. There is significant real gas destabilizing effect on the second-mode waves in Mach 10.0 oxygen flow over a flat plate. As a result, there is significant real gas effect on the second-mode receptivity to freestream disturbances in Mach 10.0 oxygen flow.

Introduction

When an aerospace vehicle travels through the atmosphere at hypersonic speed, the Mach number is high and the bow shock which envelopes the vehicle is pushed very close to the edge of the boundary lay. The shock converts the kinetic energy of the stream to internal energy, raising the temperature to a value where real gas effects due to excitation of vibrational energy and chemical reaction are required to be considered. Therefore, the receptivity and stability of thermochemical nonequilibrium hypersonic flow is much more complicated than supersonic flow. For chemical reaction with five species (N_2, O_2, NO, N, O) without ionization, at least 17 reactions [1–3] need to be modeled, which cost more memory and CPU time in numerical simulations because much more variables need to be considered compared with simulation of perfect gas flow. In addition, for general thermochemical nonequilibrium flow, time scales associated with finite rates of internal energy relaxation and reaction cause more strict limit on CFL number in time

*Graduate Student Researcher, Department of Mechanical and Aerospace Engineering

†Professor, Department of Mechanical and Aerospace Engineering, Associate Fellow AIAA.

step for stable numerical simulations. Therefore, on one hand, it is computationally very expensive for simulation of thermochemical nonequilibrium air flow. It's well known that chemical reactions in hypersonic flow have strong effect on wall temperature. According to Mack's study [4] on the effects of wall temperature, the wall cooling is stabilizing to the first mode and destabilizing to the second mode while there is no much influence on acoustic disturbances. Among reactions involving five species (N_2, O_2, NO, N, O) in air flow, some of them are endothermic and others are exothermic. Therefore, there are contrary effects on the wall temperature from chemical reactions. Thus, there are also contrary effects from chemical reactions on stability of hypersonic boundary layer based on Mack's results [4]. Thus, on the other hand, it might be very difficult to analyze the result about receptivity and stability of hypersonic thermochemical nonequilibrium air flow from numerical simulations if there exists complicated and contrary effects in the simulations. For these two reasons, as an expediency, a Mach 10.0 oxygen (O_2) flow over an infinite thin and semi-infinite flat plate is studied in both perfect gas and thermochemically nonequilibrium regime to study the real gas effects on the receptivity and stability of hypersonic boundary-layer flow. Qualitatively, reacting oxygen flow can keep main aspect of reacting air flow for the purpose of studying real gas effect on receptivity and stability of hypersonic boundary-layer flow. Oxygen other than nitrogen flow is considered because dissociation of oxygen takes place at much lower temperature ($T^* > 2500^\circ K$) at 1 atm pressure.

The steady flow solutions are first obtained by using combination of TVD shock-capturing method and shock-fitting method. The characteristics of boundary-layer normal modes at different frequencies are studied by both LST and DNS in perfect gas regime. At last, the mechanisms of receptivity to two different types of freestream disturbances, i.e., fast acoustic waves, slow acoustic waves, are studied in both perfect gas and thermochemically nonequilibrium regime. The effects of incident wave angles, forcing wave frequencies, on the receptivity are investigated.

Governing Equations and Physical Model

The governing equations are formulated for a two-temperature model with two species (non-ionizing) finite rate chemistry under the assumption that the rate of rotational relaxation approachs infinity, and the rotational energy is fully excited (*i.e.*, rotational temperature equals translational temperature).

In conservative form, the two-dimensional Navier-Stokes equation can be written as:

$$\frac{\partial \mathbf{U}}{\partial t} + \frac{\partial}{\partial x}(\mathbf{F_1} + \mathbf{F_{v1}}) + \frac{\partial}{\partial y}(\mathbf{F_2} + \mathbf{F_{v2}}) = \mathbf{W} \qquad (1)$$

where the conserved quantity and source term vectors are:

$$\mathbf{U} = \begin{bmatrix} \rho_1 \\ \rho_2 \\ \rho u \\ \rho v \\ E_v \\ E \end{bmatrix}, \qquad \mathbf{W} = \begin{bmatrix} w_1 \\ -w_1 \\ 0 \\ 0 \\ w_v \\ 0 \end{bmatrix}. \qquad (2)$$

Inviscid fluxes are

$$\mathbf{F_1} = \begin{bmatrix} \rho_1 u \\ \rho_2 \\ \rho u^2 + p \\ \rho uv \\ uE_v \\ u(E+p) \end{bmatrix}, \quad \mathbf{F_2} = \begin{bmatrix} \rho_1 v \\ \rho_2 v \\ \rho uv \\ \rho v^2 + p \\ vE_v \\ v(E+p) \end{bmatrix}. \qquad (3)$$

Viscous and diffusive fluxes are

$$\mathbf{F_{v1}} = \begin{bmatrix} j_{1x} \\ j_{2x} \\ -\tau_{xx} \\ -\tau_{xy} \\ q_{vx} \\ Q_x \end{bmatrix}, \quad \mathbf{F_{v2}} = \begin{bmatrix} j_{1y} \\ j_{2y} \\ -\tau_{xy} \\ -\tau_{yy} \\ q_{vy} \\ Q_y \end{bmatrix}. \qquad (4)$$

where

$$\begin{aligned} Q_x &= -u\tau_{xx} - v\tau_{xy} + q_x, \\ Q_y &= -u\tau_{xy} - v\tau_{yy} + q_y. \end{aligned} \qquad (5)$$

Flow Conditions of Mach 10 Oxygen Flow over a Flat Plate

The flow conditions are:

$M_\infty = 10$ $\qquad$ $T^*_\infty = 350.0\ K$

$p^*_\infty = 3903.5Pa$ $\qquad$ $Pr = 0.72$

$Re^*_\infty = \rho^*_\infty u^*_\infty / \mu^*_\infty = 6.6 \times 10^6/m$

TVD shock-capturing method is used to calculated the flow in the leading edge region because there is a singular point at the tip of the leading edge which could not be dealt with high order shock-fitting methods. The flow domain for TVD calculation is between $-0.0006 < x^* < 0.0064m$ and the body of wedge start at $x^* = 0.0m$. Uniform grids with $\triangle x^* = 3.5 \times 10^{-5}m$) and totally 200 points are used along streamwise direction, while 200 points and grid stretching function are used in wall-normal direction to cluster more points inside the boundary layer near the wall.

The TVD solutions of the flow in the leading edge region are then used as inflow conditions to start the simulation by the fifth-order shock-fitting method. The computational domain of the shock-fitting method ranges from $x^* = 0.003985m$ ($Re_x = 26301$) to $x^* = 0.8284M$ ($Re_x = 5.47 \times 10^6$). The computational domain is divided into 13 zones along streamwise direction with a total of 2536 grid points and 121 points in the wall-normal direction. Uniform grids are used in streamwise direction, while grid stretching function is used in

wall-normal direction to cluster more points inside the boundary layer near the wall.

Adiabatic noncatalytic wall boundary condition is used for steady flow calculation, while temperature perturbations and disturbance of dissociation on the wall surface are set to be zero for unsteady calculations.

Steady base flow solutions

Figure 1 compares the shock position and distribution of Mach number behind the shock between nonequilibrium flow and perfect gas flow. It shows that the oblique shock is pushed a little bit more close to the wall and Mach number immediately behind the shock is larger due to weaker oblique shock for nonequilibrium flow compared with perfect gas flow.

Figure 2 compares distribution of pressure along the wall surface. Due to a little bit stronger shock in perfect gas flow, pressure on the wall is larger than that in nonequilibrium flow. The wall temperature of base flow is shown in Fig 3. The wall temperature is almost constant for perfect gas while the vibrational temperature is in nonequilibrium with translational temperature and becomes close to each other in the downstream in reacting flow. Wall temperature of nonequilibrium flow is much lower than that of perfect gas flow because the reaction is endothermic. The comparison of temperature profile located at $x^* = 0.2m$ ($R = 1148.9$) is plotted in Fig 4. It shows that vibrational temperature is in nonequilibrium with translational temperature inside the boundary layer for reacting flow. It is obvious that the thickness of boundary layer for perfect gas is larger than reacting flow, which is also shown in streamwise velocity profile at the same location plotted in Fig. 5. The thickness of boundary layer shown in Fig. 5 is about $\delta/L = 32.0$ for perfect gas, while it is only 27.1 for reacting flow. As a result, it may change the property of the second-mode disturbance because the wavelength of second mode is proportional to boundary layer thickness [5]. Figure 6 compares pressure profile located at $x^* = 0.2m$ ($R = 1148.9$). There are great gradients in pressure profiles outside the boundary layer due to strong interaction between inviscid external flow and viscous boundary-layer flow.

Figure 7 shows the distribution of mass fraction of dissociation. In this case, the maximum mass fraction of dissociated O_2 is 7.7%, which occurs on the wall near the outlet. Figure 8 shows the profile of mass fraction of dissociated oxygen at $x^* = 0.2m$. It shows that dissociation mainly takes place near the wall.

Boundary-Layer Wave Mode Characteristics

From our previous studies on characteristics of boundary-layer normal modes, it is found that phase velocities of different boundary-layer normal modes or growth rates of the second mode are functions of the product of the local Reynolds number (R) and frequency (F). For different frequencies, almost the same distributions of phase velocities of boundary-layer normal modes and growth rates of the second mode *vs* $R*F$ are obtained In this section, characteristics of boundary-Layer normal modes of Mach 10.0 oxygen flow over a flat plate is studied by both LST and DNS in perfect gas regime.

Boundary-Layer Wave Mode Characteristics by LST

The boundary-layer wave mode characteristics of Mach 10.0 oxygen flow over the flat plate is first studied by the LST based on the steady flow solutions of perfect gas.

Figure 10 compares distributions of phase velocities of boundary-layer discrete modes, i.e., mode I and Mack modes at different locations in terms of ω ($\omega = R*F$). Two different fixed frequencies, $F = 5.0 \times 10^{-5} (f^* = 187.4kHz)$ and $F = 3.98 \times 10^{-5} (f^* = 149.2kHz)$ are studied. Phase velocities of fast acoustic waves $(1+1/M_\infty)$, entropy/vorticity wave (1), and slow acoustic waves $(1 - 1/M_\infty)$ are also shown in the figure for comparison. It shows that the phase velocity of mode I approaches that of fast acoustic waves with decreasing ω, while phase velocity of Mack mode approaches that of slow acoustic waves near the leading edge. There are contrary trends for phase velocity change of mode I and Mack mode. Specifically, phase velocity of mode I decreases with increasing ω, while that of Mack mode increases during propagation downstream (or increasing ω). There is a gap in the phase velocity curve of mode I, which leads to two branches of distributions of mode I waves. With increasing ω, the phase velocity of mode I passes across the phase velocity curve of Mack modes. At the intersection point ($\omega = 0.0619$), mode I gets synchronized with the second mode, where both modes have very similar profiles of eigenfunctions. Figure 10 also shows that the distribution of phase velocities of boundary-layer wave modes is a function of the product of the local Reynolds number (R) and frequency (F). Again, almost the same distributions of phase velocities of boundary-layer wave modes *vs* ω ($\omega = R*F$) are obtained for two different frequencies.

Figure 11 shows the growth rates of boundary-layer normal modes *vs* ω for two different frequencies. Again, the growth rate curves for different normal modes, especially for second mode of most interest, are very close to each other for the two frequencies. While the growth rates of Mack modes are continuous, there is a gap in the growth rate curves for mode I. It also shows that mode I is stable, while Mack modes is stable or slightly unstable before the synchronization with mode I ($\omega < 0.0619$). The Mack mode in this range is the conventional first mode. When $\omega > 0.0619$, the Mack mode is the conventional second mode, It's obvious that the first mode and second mode are in fact different sec-

tions of a single Mack mode. The growth rates of the second mode change dramatically. Peak growth rate of the second mode is obtained at $\omega = 0.0675$ with value $\alpha_i = -0.00163$.

Figure 9 shows the neutral curve of Mack modes for Mach 10.0 oxygen flow over the flat plate. The critical local Reynolds number (R) for boundary-layer instability is about 200. In reality, the frequency band of dominant environmental noise in experiment or flight conditions is between $10KHz$ and $300kHz$. It shows that there is absence of second-mode Branch II neutral point in the computational domain at even very high frequency with frequency $f^* = 304.5kHz$ ($F = 0.8125 \times 10^{-4}$). This means the second-mode waves will keep growing in the computational domain once they are generated at this frequency or frequencies lower than this ($F = 0.5 \times 10^{-4}$, for example).

Boundary-Layer Wave Mode Characteristics by DNS

After the characteristics of boundary-layer discrete modes of Mach 10.0 oxygen flow over the flat plate are studied by the LST, they are reconsidered by numerical simulations to compare with LST results. The numerical simulations are based on solving the full Navier-Stokes equations, which are able to capture all effects that neglected by the LST, such as, nonparallel effects of the boundary layer, the resonant interactions between different wave modes, and the effects of the oblique shock. Therefore, it is expected to obtain more reliable results about the characteristic of boundary-layer normal modes compared with LST results. Here, the characteristics of Mack-mode waves and mode I waves, including development of wave structure, change of phase velocity, growth rates, mode change and resonant interactions are studied in numerical simulations by introducing pure boundary-layer discrete modes from the inlet. The profile of discrete modes are obtained from the LST. At the inlet boundary of the computational domain, the flow is specified as the superposition of the steady base flow and a temporal fluctuations of flow variables with multiple frequencies ω_n, amplitude ϵ, and streamwise wave number α_r with the form

$$\phi(x_{in}, y, t) = \bar{\phi}(x_{in}, y) + \Re\{\epsilon \sum_{n=0}^{N} \hat{\phi_n}(y) e^{i(\alpha_{rn} x_{in} - n\omega_1 t)}\}\ , \quad (6)$$

where $\phi(x_{in}, y, t)$ represents any of the flow variables, $\hat{\phi_n}(y)$ is profile of disturbances for boundary-layer discrete modes obtained from the LST.

In the current test cases, a total of 15 frequencies ($N = 15$), with the lowest frequency of $f_1^* = 14.92kHz$, corresponding to dimensionless frequency of $F_1 = 3.98 \times 10^{-6}$, and highest frequency of $f_15^* = 223.8$ ($F_{15} = 59.7 \times 10^{-6}$), are considered in numerical simulations. Higher frequencies are integer times of the lowest frequency, *i.e.*, $f_n^* = nf_1^*$, and $F_n = nF_1$. The profiles of disturbances of boundary-layer normal modes from the LST are normalized by pressure perturbations on the wall. Therefore, the amplitude of pressure perturbations on the wall of the inlet are same for different frequencies. The factor ϵ to control the total amplitudes of forcing disturbances is carefully chosen so that the nondimensional amplitudes of the perturbations are at least one order of magnitude larger than that of the maximum numerical noise, and they are small enough to preserve the linearity of boundary-layer disturbances. Here, $\epsilon = 1.0 \times 10^{-6}$ is used, which has been demonstrated in numerical tests to keep the linearity of boundary-layer disturbances studied in this section. The subsequent downstream propagation of boundary-layer normal modes are simulated by time-accurate computations of the full Navier-Stokes equations. The unsteady calculations are carried out until the solutions reach a periodic state in time. Temporal Fourier analysis is carried out on local perturbations of unsteady flow variables to decompose boundary-layer wave modes with different frequencies. The phase velocity and growth rates of boundary-layer disturbances are calculated based on the results from Fourier analysis.

Behavior of Mack modes

Figure 12, 13 and 14 compare amplitudes of pressure perturbations along the wall surfaces between different frequencies, when the first-mode waves are introduced to the flow field from the inlet at $x_{in}^* = 0.07401m$ ($R_{in} = 698.9$). The initial amplitudes of pressure perturbation of the first-mode waves at the inlet have the same value 1.4×10^{-4} for different frequencies. Mack-mode waves at low frequencies within $n \leq 3$ decay after the inlet, while Mack-mode waves at middle frequencies and high frequencies within $n \geq 4$ are amplified in different degrees although there are some decay at the beginning for frequencies with $n = 4, 5, 6$. The decay of Mack-mode waves at low frequencies and the decay of Mack-mode waves near the inlet for middle frequencies ($n = 4, 5, 6$), are due to stable properties of the first mode with small ω shown in Fig. 11. Among Mack-mode waves with different frequencies, boundary-layer disturbances at frequency with $n = 8(119.4kHz)$ are most amplified. From the neutral curve of Mack mode shown in Fig. 9, the second-mode Branch II neutral points should be absent for all frequencies because the highest frequency considered here (0.597×10^{-4}) is lower than the straight line with $F = 0.8125 \times 10^{-4}$) shown in Fig. 9. However, there are second-mode Branch II neutral points shown in Fig. 13 and 14 for frequencies between $9 \leq n \leq 15$. In our previous study on Mach 4.5 flow and Mach 8.0 flow, the second-mode waves decay and die down very fast after they pass the second-mode Branch II neutral points. However, for current case of Mach 10.0 flow over the flat plate shown in Fig. 13 and

Table 1: Second-mode waves at Branch II neutral point ($R_{in} = 698.9$).

n	f_n^* (kHz)	K_{gn}	$s_{II}^*(m)$	ω_{II}
9	134.3	16.4	0.6414	0.07652
10	149.2	12.3	0.5622	0.07667
11	164.1	9.61	0.4603	0.07631
12	179.1	7.75	0.3901	0.07663
13	194.0	6.39	0.3311	0.07649
14	208.9	5.33	0.2871	0.07670
15	223.8	4.77	0.2529	0.07712

Table 2: Second-mode waves generated from mode I waves ($R_{in} = 698.9$).

n	f_n^* (kHz)	K_{gn}	$s_{II}^*(m)$	ω_{II}
9	134.3	0.50	0.7400	0.0792
10	149.2	1.31	0.5739	0.0775
11	164.1	1.64	0.4599	0.0763
12	179.1	1.46	0.3706	0.0747
13	194.0	1.07	0.3198	0.0752
14	208.9	0.71	0.2797	0.0757
15	223.8	0.47	0.2464	0.0761

14, the second-mode waves do not die down after passing the second-mode Branch II neutral point. Instead, they are gradually amplified again after a little decay. One possible reason for growth of Mack modes is that the third unstable Mack mode is generated from the second Mack mode. However, Mack modes in the growth region after Branch II neutral points are identified to be still the second mode by comparing with the LST results. Therefore, the reason for failure in prediction of the existence of the second-mode Branch II neutral points at frequencies lower than $F = 0.8125 \times 10^{-4}$ is not clear. There is visible numerical noise in distribution of disturbance amplitude in downstream region after $x^* > 0.5m$, which may be due to oscillation of the shock induced by strongly amplified second-mode waves.

Table 1 provides growth ratios (ratio of the second-mode amplitude at Branch II neutral points and initial amplitude at the inlet) and locations of the second-mode Branch II neutral points (x_{II}^* or ω_{II}) for different frequencies.

From table 1, the second-mode Branch II neutral points are located at about $\omega_{II} = 0.0765$, and the relative change in terms of ω ($\omega = R * F$) from the simulations is less than %1. The growth ratio (k_g) monotonically decreases with increasing frequencies shown in O2-Tab-2nd-z3.

Behavior of mode I waves

Similar studies are carried out for mode I waves. Mode I waves with initial amplitudes 1.4×10^{-4} for pressure perturbations at different frequencies are introduced to the flow field from the same inlet at $x_{in}^* = 0.07401m$ ($R_{in} = 698.9$). Figure 15, 16 and 17 compare amplitudes of pressure perturbations along the wall surfaces between different frequencies. Compared with the behavior of Mack mode waves shown in Fig. 12, 13 and 14, there are much more complicated patterns of growth and decay during the propagation of mode I waves. There are strong oscillations in pressure perturbations for all different frequencies, which indicates there is modulation between forcing mode I waves and other waves. From pervious study on Mach 4.5 flow over a flat plate and Mach 8.0 flow over a sharp wedge, fast acoustic waves are inevitablely brought to flow field when mode I waves are introduced from the inlet near the leading edge. As a result, there are resonant interactions between mode I waves and fast acoustic waves, which lead to the growth and oscillation of mode I waves although mode I is predicted to be stable by the LST. It is found in our previous results that mode I waves can convert to Mack-mode waves during propagation. Figure 13 and 14 shows that boundary-layer disturbances at frequencies within $9 \leq n \leq 15$ reach another peak near the second-mode Branch II neutral points given in table 1. The ratio of disturbance amplitude characterized by pressure perturbations at the second-mode Branch II neutral point and initial amplitude of forcing mode I waves at the inlet is given in table 2.

Again, the second-mode Branch II neutral points in terms of ω are located at about 0.0765 for different frequencies with relative change less than %4. It also shows in table 2 that the second mode waves generated from mode I waves are much weaker compared with that shown in table 1 when the second-mode waves are introduced from the inlet. Moreover, table 1 shows that the growth ratio of the second mode decreases with increasing frequencies. However, such trend is absence from table 2.

Comparison with LST

The results about behavior of Mack-mode waves and mode I waves from numerical simulations are compared with LST for three typical frequencies, $F = 1.99 \times 10^{-5}, 3.98 \times 10^{-5}$ and $5.97 \times 10^{-5} (n = 5, 10$ and $15)$.

Figure 18 compares the phase velocities of boundary-layer disturbances at frequency $F = 1.99 \times 10^{-5} (n = 5)$ with the LST results. Good agreement is obtained in phase velocity of Mack modes between DNS and the LST except that there is strong oscillation in DNS results after the inlet due to transient effect of forcing waves at the inlet. However, for mode I waves, there are strong oscillations in phase velocity curve, which is due

to modulation between mode I waves and fast acoustic waves. As stated before, mode I waves are companied with fast acoustic waves when they are introduced near the leading edge. Moreover, both mode I waves and fast acoustic waves have very close phase velocities at the inlet location. Therefore, there is resonant interaction between mode I waves and fast acoustic waves. That's why mode I waves are modulated and amplified (see Fig. 12).

A similar analysis is carried out for the frequency with $n = 10$ ($F = 3.98 \times 10^{-5}, f^* = 149.2kHz$). Figure 19 compares the phase velocities of boundary-layer disturbances from simulations with LST results. For Mack modes, distribution of phase velocity from the simulation is close to that from LST, although there are obvious difference between them. For mode I waves, however, the distribution of phase velocity of boundary-layer disturbances from the simulation can be divided into two parts at $x^* = 0.38m$ ($R = 1583.7$). Phase velocity of disturbances induced by mode I waves can match that of mode I from LST results before $x^* = 0.38m$, and it gradually approaches that of Mack modes after this point. This can be explained as follows. The phase velocity of mode I waves gradually decreases during propagation downstream. When the phase velocity of mode I waves becomes far away from that of fast acoustic waves, there are no more resonant interactions between them, and mode I waves decay due to their inherent stable properties. Before mode I waves die out, their phase velocity gets synchronized with that of Mack modes. Both the first Mack-mode waves and mode I waves have almost the same profiles of disturbance structure across the boundary layer at the synchronization point. As a result, mode I waves convert to the Mack-mode waves in the synchronization region, which is shown in phase velocity curves in Fig. 19.

The comparison of phase velocity curves between LST results and simulation results at frequency with $n = 15$ ($F = 5.97 \times 10^{-5}$) is plotted in Fig. Fig. 20. Simulation results with Mack modes shows excellent agreement with LST results when Mack-mode waves grow again after they pass Branch II neutral point and are followed by a little decay, although much difference in phase velocity of Mack mode between LST and DNS in upstream region with $x^* < 0.35m$ is visible in Fig. 20 for unknown reason. For mode I waves introduced from the inlet, the phase velocity of boundary-layer disturbances from the simulation can match the phase velocity of mode I wave from the LST before mode I waves convert to Mack mode waves. There is good agreement in phase velocity of Mack mode waves between simulations results with different forcing waves. For high frequency with $n = 15$, mode II waves may be appear in the flow field according to phase velocity curves of boundary-layer normal modes by LST (Fig. 20). However, there is no dominant mode II waves shown based on phase velocity curves in Fig. 20.

Growth rates of boundary-layer normal modes are most important properties in the stability study. Figure 21 compares the growth rates of Mack-mode waves at three different frequencies ($n = 8, 10, 15$) from numerical simulations with the LST results. However, there is much difference in growth rates between LST and simulation results, although the peak growth rates are still close to each other. The reason for the difference may be due to the effect of oblique shock and parallel flow assumption in the LST. In current case of Mach 10.0 flow over a flat plate, the shock is pushed very close to the wall surface. As a result, there are strong interaction between external inviscid flow including oblique shock and viscous boundary-layer flow, which is neglected by the LST. DNS accounts for both nonparallel effect and interaction between inviscid flow and viscous boundary-layer flow, so the growth rates from the results of DNS should be more reliable.

Receptivity to Freestream Acoustic Waves

After studying the characteristics of boundary-layer normal modes, freestream acoustic waves are introduced to study receptivity phenomenon that is the process how environment acoustic waves enter boundary layer and trigger boundary-layer instability waves. In this section, receptivities to both freestream fast and slow acoustic waves with different frequencies and incident angles are studied. Real gas effect on receptivity are studied by comparing the results between perfect gas and nonequilibrium flow. Boundary-layer disturbances induced from freestream acoustic waves are identified by the LST.

Freestream Planar Acoustic Waves with $\theta_\infty = 0°$ and Frequency $F = 5.0 \times 10^{-5}$

Freestream acoustic waves at frequency $F = 5.0 \times 10^{-5}$ ($f^* = 187.4kHz$) with incident angle $\theta_\infty = 0°$ are imposed at the top of computational boundary in front of the shock. The amplitude of the velocity disturbance in freestream is chosen to be $\epsilon = 1.0 \times 10^{-5}$. Receptivities to both planar fast and slow acoustic waves are studied in both perfect gas and nonequilibrium flow regime to investigate the real gas effect.

Figure 22 compares the receptivities to fast acoustic waves (a) and to slow acoustic waves (b) between perfect gas and nonequilibrium flow. Pressure perturbations immediately behind the shock ($j = 121$) and along the wall surface ($j = 1$) are plotted together in Fig. 22. It shows that there is no much difference for pressure perturbations behind the shock between perfect gas and nonequilibrium flow, although much differences exist on wall surface. According to our previous study on receptivity to freestream fast or slow acoustic waves in Mach 4.5 flow over a flat plate and Mach 8.0 flow over a sharp wedge, mode I waves are generated by fast

acoustic waves, while the first-mode waves are generated by slow acoustic waves. Mode I waves then convert to Mack-mode waves during propagation downstream in receptivity to fast acoustic waves. In this chapter, we mainly focus on the real gas effect on receptivity. In receptivity to fast acoustic waves, mode I waves decay to lower amplitude before convert to Mack-mode waves in nonequilibrium flow compared with perfect gas flow (Fig. 22). It also shows in Fig. 22 that there is negligible real gas effect on evolutions of the first-mode waves induced by slow acoustic waves. However, boundary-layer disturbances are more strongly amplified when then enter the second-mode unstable region in nonequilibrium flow compared with perfect gas flow. As a result, the amplitude of the second-mode waves at Branch II neutral points are much larger in nonequilibrium flow. Therefore, that real gas effect is destabilizing to the second mode while there is no obvious effect on mode I wave and first mode waves for the current cases. The destabilizing effect on the second mode from real gas is consistent with Mack's [4] results about cooling wall effect on the second-mode boundary-layer stability. Because the wall temperature in nonequilibrium flow is much lower than that in perfect gas flow as shown in Fig 3, the real gas effect is similar to wall cooling effect.

In perfect gas flow, the second-mode Branch II neutral point is located at $x^* = 0.3541m$ ($\omega = 0.07644$), while it is located at $x^* = 0.4122m$) ($\omega = 0.08247$) for nonequilibrium flow. In other words, the second-mode unstable region is longer in nonequilibrium flow compared with perfect gas flow. The response coefficients for the second mode to freestream acoustic waves are:

	Perfect gas	Nonequilibrium
Fast acoustic waves:	$K_s = 3.45$	$K_s = 4.24$
Slow acoustic waves:	$K_s = 8.59$	$K_s = 14.80$

Again, it's obvious that pressure perturbations induced by slow acoustic waves are much stronger than that by fast acoustic waves at current flow conditions. In fact, for receptivity to freestream fast acoustic waves shown in 22, receptivity of mode I waves is dominant in perfect gas flow, while dominant mode in nonequilibrium flow is the second-mode. Another observation in receptivity to slow acoustic waves shown in Fig. 22 is growth of the second-mode waves following the decay after passing Branch II neutral point in perfect gas flow. Therefore, maximum amplitude of the second-mode waves is not definitely located at Branch II neutral point in perfect gas flow. However, such growth after Branch II neutral point does not appear in receptivity to freestream slow acoustic waves for nonequilibrium flow. Instead, the second-mode waves decay a little after passing Branch II neutral point, then become neutral waves, i.e., amplitude of the second-mode waves is almost constant.

The mechanism of generation of different boundary-layer normal modes by fast acoustic waves and slow acoustic waves are clearly shown in distribution of phase velocity of boundary-layer disturbances presented in Fig. 23. The receptivity mechanisms of perfect gas are analyzed first. The results of nonequilibrium flow are compared with that of perfect gas flow to investigate real gas effect. The phase velocities of boundary-layer normal modes from the LST are compared with the results from DNS. In receptivity to freestream fast acoustic waves, the phase velocity of boundary-layer disturbances near the leading edge from the simulation is close to that of mode I from the LST, which indicates that mode I waves are generated by fast acoustic waves. From our previous study on characteristics of boundary normal modes, mode I waves are amplified due to resonant interactions with the forcing fast acoustic waves because their phase velocities are very close to each other near the leading edge. During propagation downstream, the phase velocity of mode I waves gradually decreases. When phase velocities of mode I waves decrease to a certain value and there is no more resonant interaction between mode I waves and fast acoustic waves ($x^* > 0.21m$), mode I waves decay due to their inherent stable properties. Before they die out, mode I waves convert to the Mack-mode waves in the synchronization region between mode I waves and the first-mode waves. Mack-mode waves generated by mode I waves are amplified again due to the instability of Mack-mode waves. On the other hand, in receptivity to freestream slow acoustic waves, the first Mack mode waves are generated due to resonant interactions between the first-mode waves and the forcing slow acoustic waves. Due to slightly unstable property of the first-mode waves and significantly unstable property of the second-mode waves, boundary-layer disturbances generated from the slow acoustic waves are strongly amplified. Due to different receptivity mechanisms shown in Fig. 23, boundary-layer disturbances induced by slow acoustic waves are much stronger than that by fast acoustic waves at current flow conditions. Specifically, mode I waves are generated in receptivity to fast acoustic waves while the first Mack mode waves are generated by slow acoustic waves near the leading edge. Mode I waves are much stable than the first Mack mode. As a result, the initial amplitude of the second Mack mode converted from mode I waves is much weaker than that from the first Mack mode. Therefore, the peak amplitude of the second mode waves are much weaker in receptivity to fast acoustic waves compared with that to slow acoustic waves. Figure 23 also shows very similar phase velocity curves of boundary-layer disturbances between perfect gas flow and nonequilibrium flow, which indicates that real gas effect does not change the receptivity mechanisms of hypersonic boundary layer.

Figure 24 compares the structure of boundary-layer disturbances induced by slow acoustic waves at station $x^* = 0.81m$ ($R = 1207.6$) with profiles of the second-mode waves. There is excellent agreement between re-

sults from the simulation and LST. This result also identifies the growing disturbances in downstream after passing Branch II neutral point to be the second-mode waves.

Effect of Incident Angles on Receptivity to Planar Freestream Acoustic waves

After studying real gas effect on receptivity to freestream acoustic waves with zero incident angle, the effect of incident acoustic wave angles on receptivity to both planar freestream fast acoustic waves and planar freestream slow acoustic waves is studied at frequency $F = 5.0 \times 10^{-5}$. Freestream acoustic waves with four different incident angles, i.e., $\theta_\infty = 0°, 22.5°, 45°$ and $67.5°$ are considered. The amplitude of the velocity disturbance in freestream is chosen to be $\epsilon = 1.0 \times 10^{-5}$. Real gas effect are investigated in all four cases with different incident angles.

Figure 25 compares amplitudes of pressure perturbations along the wall surface due to planar freestream fast acoustic waves with different incident angles. Unfortunately, there are strong oscillations in amplitudes of pressure perturbations for different incident angles due to modulation between boundary-layer disturbances and forcing waves. Furthermore, there are no clear dominant second-mode waves shown in Fig. 25 for different incident angles except for $\theta_\infty = 0°$. The real gas effect is not clear in Fig. 25 due to strong oscillations in disturbance amplitude. Fig. 25 also shows that it is difficult to obtain the second-mode growth rates by studying evolution of boundary-layer disturbances induced by freestream fast acoustic waves due to absence of dominant second mode.

Figure 26 compares amplitudes of pressure perturbations along the wall surface due to planar freestream slow acoustic waves with different incident angles. Both perfect gas flow and nonequilibrium flow are considered. The general trend of boundary-layer disturbances by freestream slow acoustic waves are very similar between perfect gas flow and nonequilibrium flow for different incident angles. The comparison of the second-mode response coefficients to freestream acoustic waves with different incident angles is plotted in Fig. 27. It shows that receptivity to slow acoustic waves drop dramatically with increasing incident angle. In addition, the second-mode response coefficients are larger in nonequilibrium flow compared with perfect gas flow. It should be noted that the second-mode response coefficients shown in Fig. 27 for perfect gas flow are ratios between amplitude of pressure perturbations at the second-mode Branch II neutral point and that in freestream acoustic waves, but not ratio between the maximum second-mode amplitude and that of freestream disturbances.

Table 3: Acoustic wave components in the freestream.

n	f_n^* (kHz)	$F_n * 10^6$	A_n	$\phi_n(radian)$
1	14.92	9.63	0.7692	2.4635(-6)
2	29.84	19.26	0.4162	0.1600
3	44.77	28.89	0.2827	2.2149
4	59.68	38.52	0.2065	4.1903
5	74.61	48.15	0.1707	6.0510
6	84.53	57.78	0.1406	5.2671
7	104.5	67.41	0.1132	2.1070
8	119.4	77.04	9.7164(-2)	5.7511
9	134.3	86.67	0.1081	5.0005
10	149.2	90.35	9.0781(-2)	5.2319
11	164.1	96.30	7.7722(-2)	2.1679
12	179.1	115.56	5.8428(-2)	5.4738
13	194.0	125.19	5.0729(-2)	0.5649
14	208.9	134.82	7.6987(-2)	5.5812
15	223.8	144.45	5.7108(-2)	4.4043

Freestream Planar Acoustic Waves with Different Frequencies

In this section, hypersonic boundary-layer receptivity to free-stream acoustic disturbances with different frequencies is studied in both perfect gas flow and nonequilibrium flow regime for Mach 10.0 oxygen flow over the flat plate. Both freestream planar fast and slow acoustic waves at $\theta_\infty = 0°$ contain 15 frequencies with the lowest frequency of $f_1^* = 14.922kHz$ corresponding to dimensionless frequency of $F_1 = 3.98 \times 10^{-6}$. The perturbations of an arbitrary flow variable in the freestream satisfy relation of acoustic waves. The relative amplitude and phase angle of acoustic waves at different frequencies are given in in table 3. The overall wave amplitude is $\epsilon = 1.0 \times 10^{-4}$ with 15 frequencies ($N = 15$).

The unsteady calculations are carried out until the solutions reach a periodic state in time. Temporal Fourier analysis is carried out on local perturbations of unsteady flow variables after a time periodic state has been reached. The Fourier transform for the real disturbances is used to extract the local perturbation amplitude and phase angle for different frequencies.

Receptivity to fast acoustic waves at different frequencies

Figure 28, 29 and 30 presents pressure perturbations along the wall surface induced by planar freestream fast acoustic waves at $\theta_\infty = 0°$ with different frequencies. Perfect gas flow is compared with nonequilibrium flow. From previous analysis in section , mode I waves are generated and amplified by resonant interaction with forcing freestream fast acoustic waves. For low frequencies within $n \leq 5$, boundary-layer disturbances are dominated by mode I waves and Mack-mode waves are

absent because Mack-mode waves are converted from mode I waves in receptivity to fast acoustic waves and the synchronization point between mode I and Mack mode is outside the computational domain for low frequencies (see Fig. 18). For middle frequencies within $6 \leq n \leq 10$, mode I waves begin to decay earlier and drop off to a lower level in nonequilibrium flow compared with perfect gas flow at the same frequency. After mode I waves convert to the second-mode waves ($7 \leq n \leq 10$), boudary-layer disturbances are more strongly amplified in nonequilibrium flow, especially for frequencies with $n = 9, 10$. With increase frequency, there are more strong oscillations in boundary-layer disturbances due to modulation with forcing fast acoustic waves. This is because the result of modulation between different waves are related to wave length of different waves involved in the modulation. As a result of modulation, new wave component at even higher frequency with shorter wave length is generated. For high frequencies within $11 \leq n \leq 15$, the evolution of boundary-layer disturbances are contaminated by wave modulation. Again, it is found that there is no clear evolution of the second-mode disturbances shown in receptivity to freestream fast acoustic waves in both equilibrium flow and perfect gas flow.

Receptivity to slow acoustic waves at different frequencies

Figure 31, 32 and 33 compares pressure perturbations along the wall surface induced by planar freestream fast acoustic waves at $\theta_\infty = 0°$ with different frequencies in both perfect gas flow and nonequilibrium flow. Overall, there are much cleaner evolutions of boundary-layer disturbances induced by freestream slow acoustic waves compared with that generated by fast acoustic waves. From receptivity mechanisms discussed in section , the first-mode waves are generated near the leading edge in the receptivity process to freestream slow acoustic waves. At frequencies within $n \leq 8$, the first-mode waves generated by freestream slow acoustic waves are less amplified in nonequilibrium flow compared with those in perfect gas flow. In other words, real gas effect is stabilizing to the first-mode waves, which is also consistent with Mack's [4] results about cooling wall effect on the first-mode boundary-layer stability. However, at high frequencies within $n \geq 9$ or $F \geq 3.58 \times 10^{-5}$, such stabilizing effect from real gas to the first-mode waves are invisible in Fig. 22, 32 and 33. Therefore, real gas effect on stability of the first mode depenps on frequency. Specifically, real gas is stabilizing to the first mode for frequencies within $n \leq 8$, while it has no much effect on the first mode for higher frequencies within $n \geq 9$. Moreover, the second-mode waves at frequencies within $n \geq 9$ are more strongly amplified in nonequilibrium flow due to destabilizing effect from real gas on the second mode. As a result, there is no

Table 4: Response coefficients of the second mode to freestream slow acoustic waves.

–	Perfect gas			Nonequilibrium flow		
n	K_s	$x^*_{II}(m)$	ω_{II}	K_s	$x^*_{II}(m)$	ω_{II}
9	22.9	0.7031	0.0772	-	-	-
10	16.0	0.5705	0.0772	24.3	0.6945	0.0852
11	12.2	0.4638	0.0766	17.7	0.5570	0.0839
12	9.70	0.3918	0.0768	15.4	0.4664	0.0838
13	7.84	0.3290	0.0762	10.7	0.3888	0.0829
14	6.69	0.2828	0.0761	10.7	0.3272	0.0819
15	5.80	0.2487	0.0765	8.20	0.3016	0.0842

the second-mode Branch II neutral point at frequency with $n = 9$ shown in refcomp-PR-fa-sl-00-am-px-2-JL for nonequilibrium flow, while the second-mode waves reach a peak value at Branch II neutral point located at $x^* = 0.704m$ ($R = 2154.2$) in perfect gas flow. This is because the second-mode Branch II neutral point at frequency with $n = 9$ for nonequilibrium flow is outside the computational domain. The response coefficients of the second mode are given in table 4.

Due to destabilizing effect from real gas, the second-mode response coefficients in the table 4 are larger in nonequilibrium flow compared with perfect gas flow. The second-mode Branch II neutral point is located at about $\omega_{II} = 0.0767$ with relative change in simulations less than %1 for perfect gas, while it is located about $\omega_{II} = 0.0836$ with relative change less than %2.1 for nonequilibrium flow. In addition, the second-mode response coefficients decrease as frequency increases, which is also shown in Figure 34.

Conclusions

The real gas effect on receptivity of hypersonic boundary layer to freestream fast acoustic waves for a Mach 10 oxygen flow over a flat plate has been studied by both numerical simulations and linear stability analyses. It is found that there is strong real gas effect on the second-mode receptivity of reacting oxygen flow to freestream acoustic waves. Compared with results of perfect gas, the unstable region for nonequilibrium flow is longer and the peak amplitude is larger, which means that the real gas effect is destabilizing for the discrete modes in this region.

Acknowledgements

This research was supported by the Air Force Office of Scientific Research, USAF, under AFOSR Grand # F49620-00-1-0101. The program manager is Dr. John Schmisseur. The views and conclusions contained herein are those of the author and should not be interpreted as necessarily representing the official policies or endorsements either expressed or implied, of the Air

Force Office of Scientific Research or the U.S. Government.

References

[1] C. Park. On convergence of chemically reacting flows. *AIAA Paper 85-0247*, 1985.

[2] Goulard R. On catalytic recombination rates in hypersonic stagnation heat transfer. *Jet Propulsion*, 28(11):733–745, 1958.

[3] C. Park. *Nonequilibrium Hypersonic Aerothermodynamics*. Wiley Interscience, 1990.

[4] L. M. Mack. Stability of Axisymmetric Boundary Layers on Sharp Cones at Hypersonic Mach Numbers. *AIAA Paper 87-1413*, 1987.

[5] M. L. Hudson, N. Chokani, and G. V. Candler. Nonequilibrium effects on hypersonic boundary layers and inviscid stability. *AIAA Paper 94-0825*, 1994.

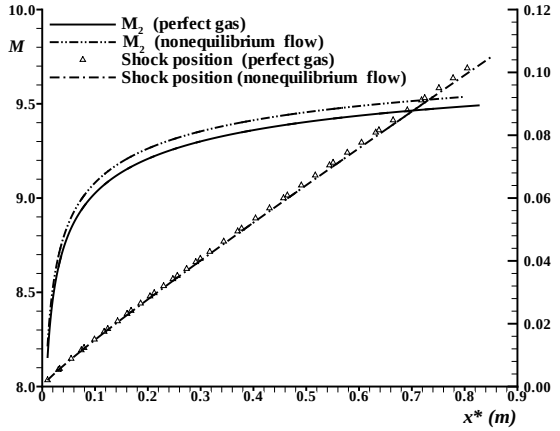

Figure 1: Shock position and distribution of Mach number behind the shock for steady oxygen flow over a flat plate ($M_\infty = 10.0$, $Re^*_\infty = 6.6 \times 10^6/m$).

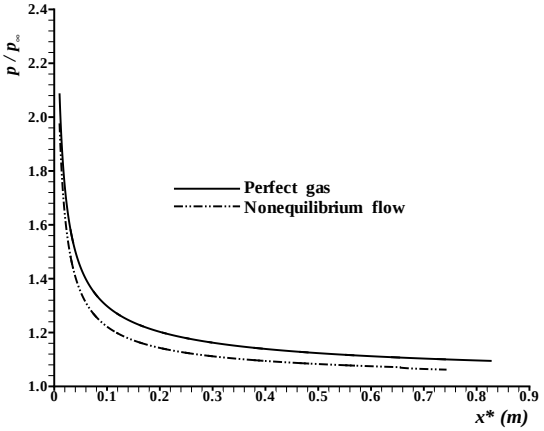

Figure 2: Distribution of pressure along the wall surface for steady oxygen flow over a flat plate ($M_\infty = 10.0$, $Re^*_\infty = 6.6 \times 10^6/m$).

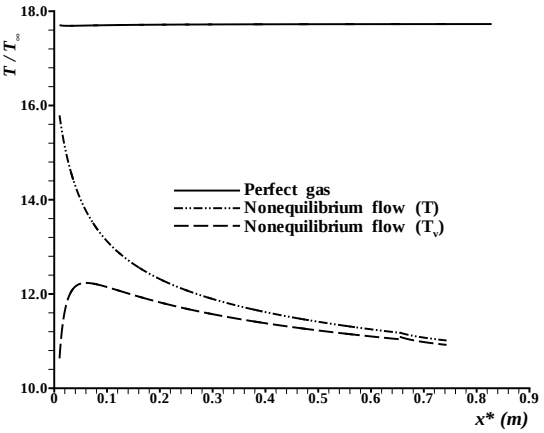

Figure 3: Distribution of wall temperature for steady oxygen flow over a flat plate ($M_\infty = 10.0$, $Re^*_\infty = 6.6 \times 10^6/m$).

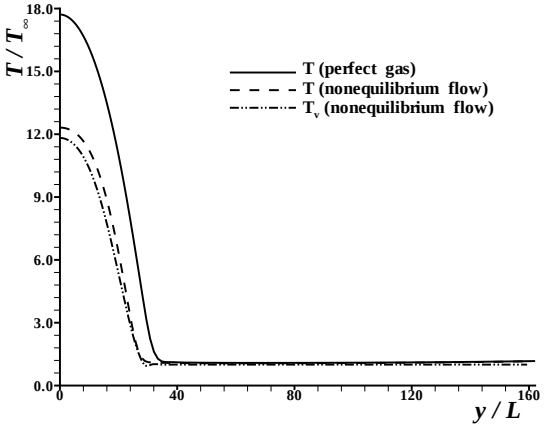

Figure 4: Profiles of temperature for steady oxygen flow over a flat plate ($M_\infty = 10.0$, $Re^*_\infty = 6.6 \times 10^6/m$, $x^* = 0.2m$ and $R = 1148.9$).

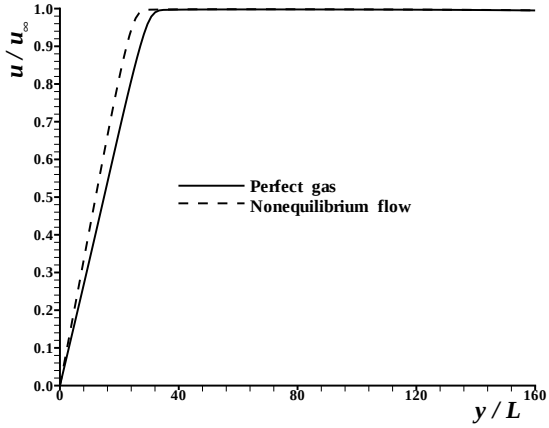

Figure 5: Profiles of streamwise velocity for steady oxygen flow over a flat plate ($M_\infty = 10.0$, $Re^*_\infty = 6.6 \times 10^6/m$, $x^* = 0.2m$ and $R = 1148.9$).

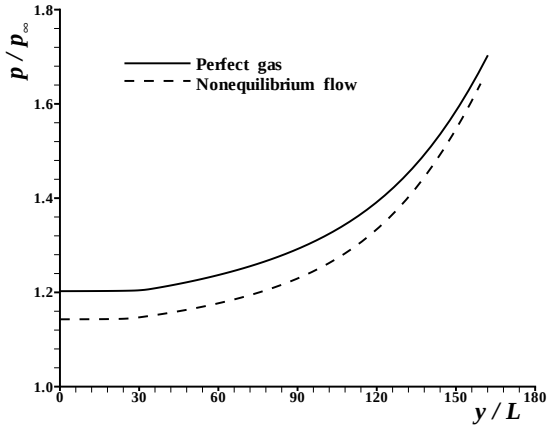

Figure 6: Profiles of pressure for steady oxygen flow over a flat plate ($M_\infty = 10.0$, $Re^*_\infty = 6.6 \times 10^6/m$, $x^* = 0.2m$ and $R = 1148.9$).

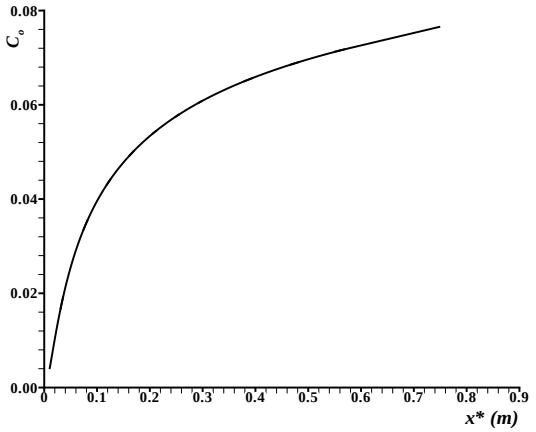

Figure 7: Distribution of mass fraction of elemental oxygen for steady oxygen flow over a flat plate ($M_\infty = 10.0$, $Re^*_\infty = 6.6 \times 10^6/m$).

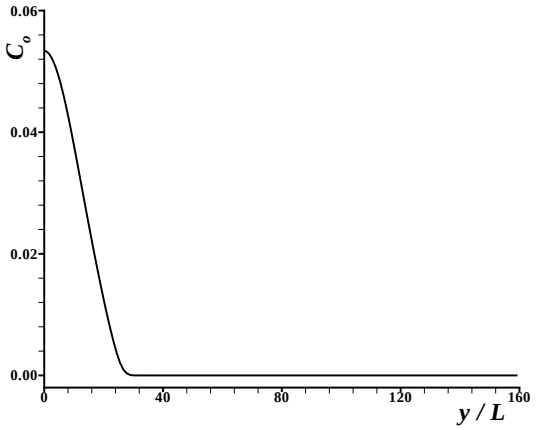

Figure 8: Profiles of mass fraction of dissociated oxygen for steady oxygen flow over a flat plate ($M_\infty = 10.0$, $Re^*_\infty = 6.6 \times 10^6/m$, $x^* = 0.2m$ and $R = 1148.9$).

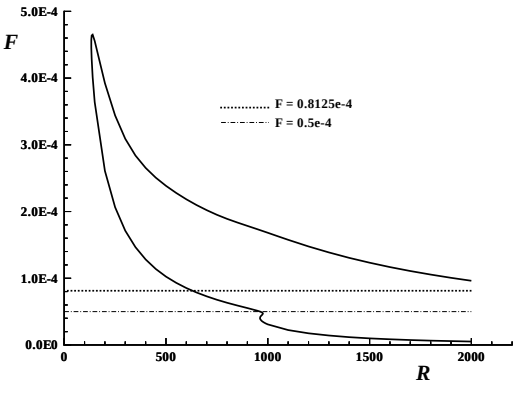

Figure 9: Neutral stability curves of two-dimensional first and second modes in the hypersonic oxygen flow over a flat plate ($M_\infty = 10.0$, $Re^*_\infty = 6.6 \times 10^6/m$).

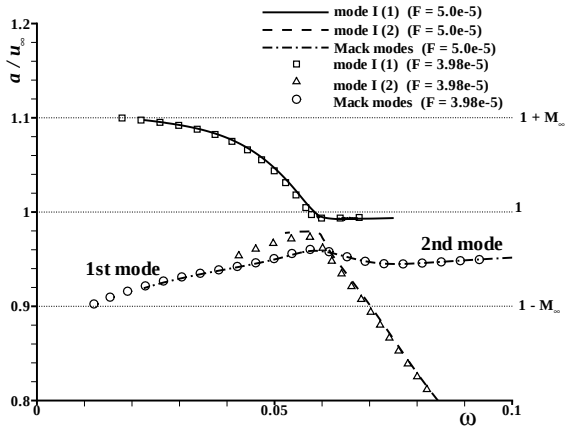

Figure 10: Distribution of phase velocities of boundary-layer normal modes as a function of ω at different frequencies in the hypersonic oxygen flow over a flat plate ($M_\infty = 10.0$, $Re^*_\infty = 6.6 \times 10^6/m$).

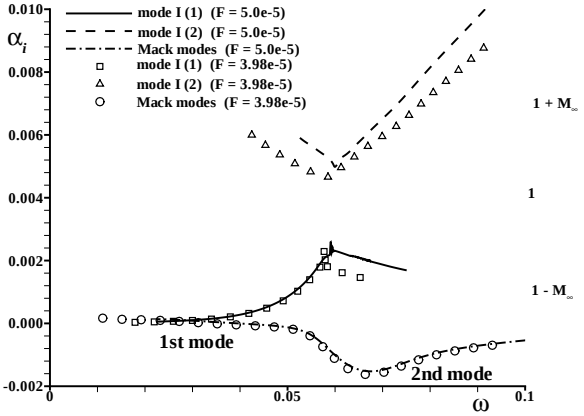

Figure 11: Distribution of growth rates of boundary-layer normal modes as a function of ω at different frequencies in the hypersonic oxygen flow over a flat plate ($M_\infty = 10.0$, $Re^*_\infty = 6.6 \times 10^6/m$).

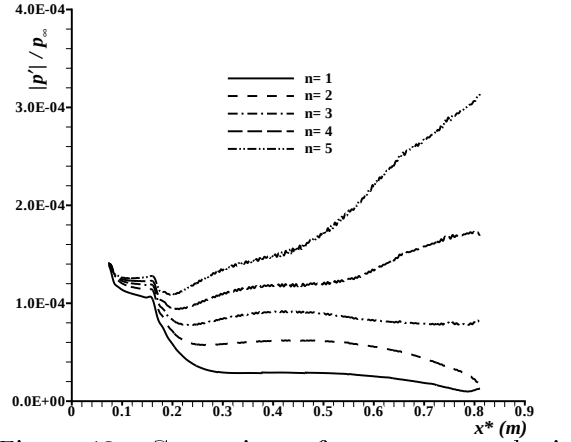

Figure 12: Comparison of presure perturbations of Mack modes along the wall surface at different frequencies in the hypersonic oxygen flow over a flat plate ($M_\infty = 10.0$, $Re^*_\infty = 6.6 \times 10^6/m$).

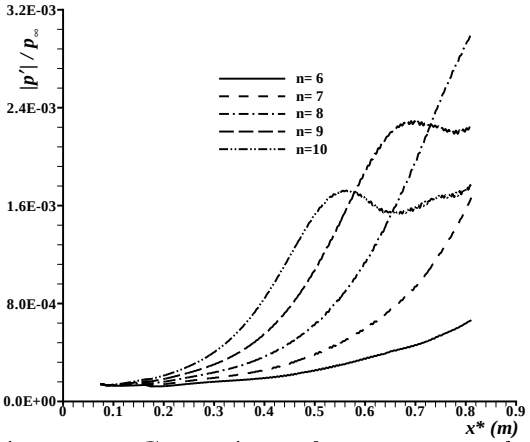

Figure 13: Comparison of presure perturbations of Mack modes along the wall surface at different frequencies in the hypersonic oxygen flow over a flat plate ($M_\infty = 10.0$, $Re^*_\infty = 6.6 \times 10^6/m$).

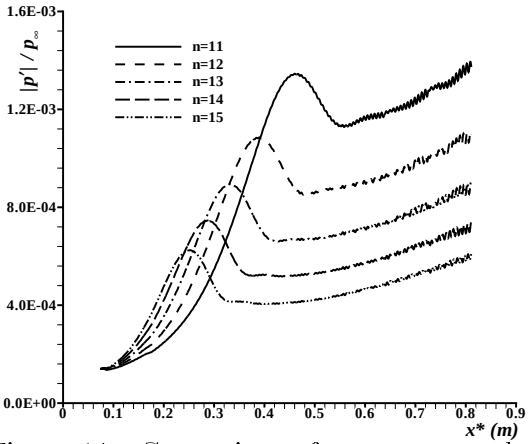

Figure 14: Comparison of presure perturbations of Mack modes along the wall surface at different frequencies in the hypersonic oxygen flow over a flat plate ($M_\infty = 10.0$, $Re^*_\infty = 6.6 \times 10^6/m$).

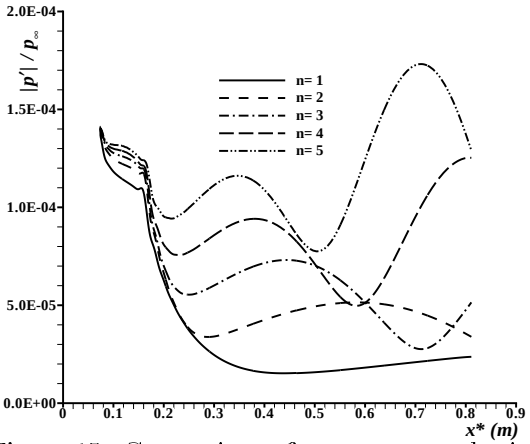

Figure 15: Comparison of presure perturbations along the wall surface for the cases of imposed mode I of different frequencies at the inlet ($M_\infty = 10.0$, $Re^*_\infty = 6.6 \times 10^6/m$).

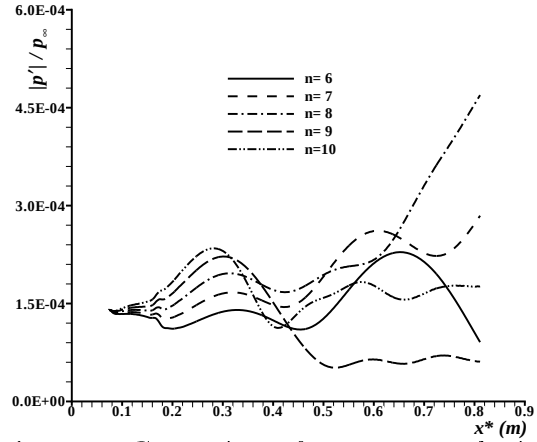

Figure 16: Comparison of presure perturbations along the wall surface for the cases of imposed mode I of different frequencies at the inlet ($M_\infty = 10.0$, $Re^*_\infty = 6.6 \times 10^6/m$).

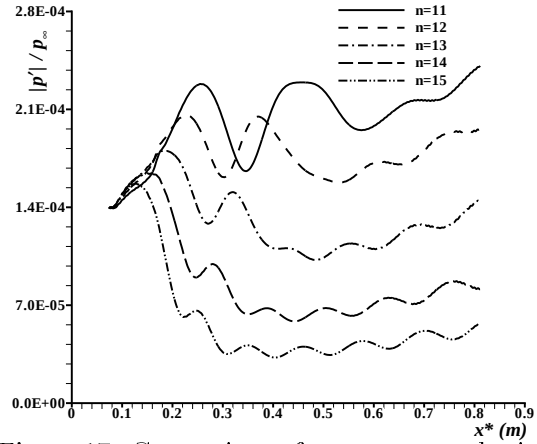

Figure 17: Comparison of presure perturbations along the wall surface for the cases of imposed mode I of different frequencies at the inlet ($M_\infty = 10.0$, $Re^*_\infty = 6.6 \times 10^6/m$).

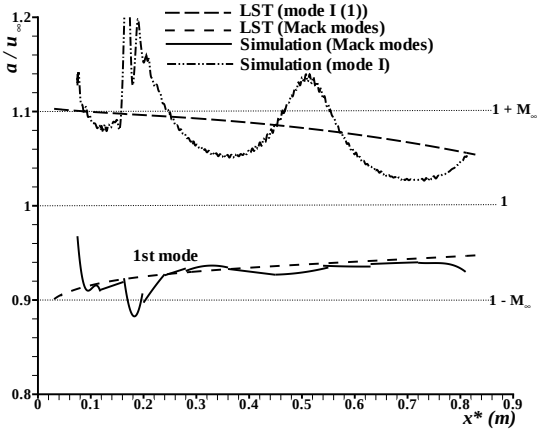

Figure 18: Comparison of phase velocities of boundary-layer normal modes from numerical simulations with LST resutls ($M_\infty = 10.0$, $Re^*_\infty = 6.6 \times 10^6/m$, and $F = 1.99 \times 10^{-5}$).

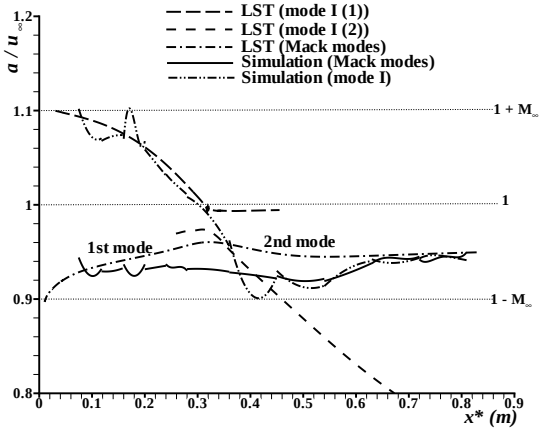

Figure 19: Comparison of phase velocities of boundary-layer normal modes from numerical simulations with LST resutls ($M_\infty = 10.0$, $Re^*_\infty = 6.6 \times 10^6/m$, and $F = 3.98 \times 10^{-5}$).

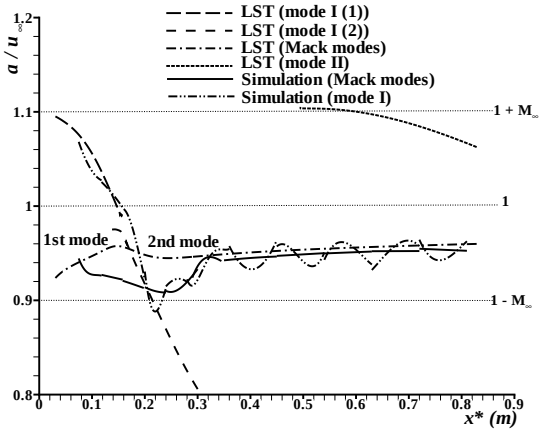

Figure 20: Comparison of phase velocities of boundary-layer normal modes from numerical simulations with LST resutls ($M_\infty = 10.0$, $Re^*_\infty = 6.6 \times 10^6/m$, and $F = 5.97 \times 10^{-5}$).

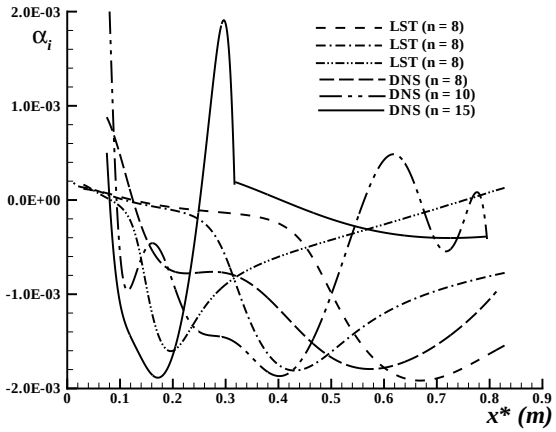

Figure 21: Comparison of growth rates of Mack modes between numerical simulation results and LST resutls ($M_\infty = 10.0$, $Re^*_\infty = 6.6 \times 10^6/m$).

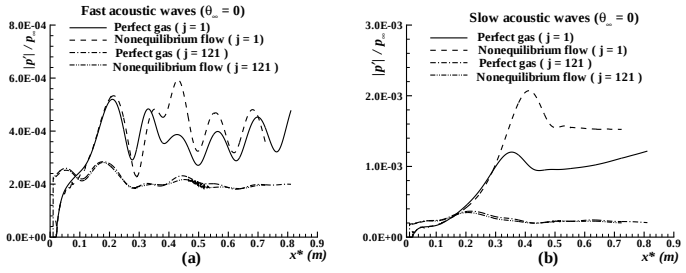

Figure 22: Distribution of pressure perturbations along the wall ($j = 1$) and immediately behind the shock ($j = 121$) due to freestream plane acoustic waves ($M_\infty = 10.0$, $Re^*_\infty = 6.6 \times 10^6/m$, $\theta_\infty = 0°$ and $F = 5.0 \times 10^{-5}$).

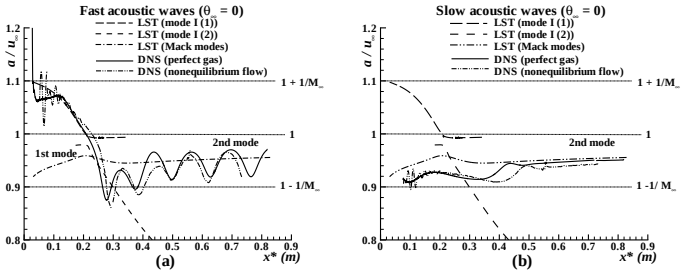

Figure 23: Distribution of phase velocities of boundary-layer disturbances due to freestream plane acoustic waves and comparison with LST results ($M_\infty = 10.0$, $Re^*_\infty = 6.6 \times 10^6/m$, $\theta_\infty = 0°$ and $F = 5.0 \times 10^{-5}$).

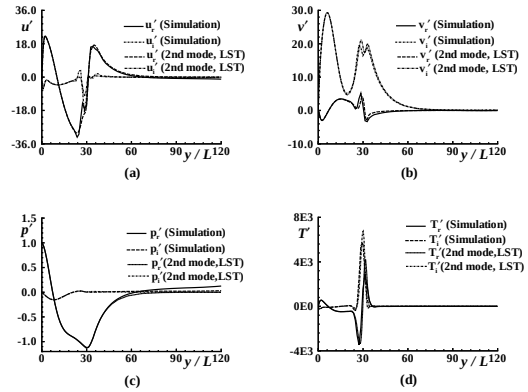

Figure 24: Comparison of the wave structures of disturbances induced by freestream slow acoustic waves and those of the second-mode disturbances of linear stability theory at $x^* = 0.81m$ ($R = 1207.6$) ($M_\infty = 10.0$, $Re^*_\infty = 6.6 \times 10^6/m$, $\theta_\infty = 0°$ and $F = 5.0 \times 10^{-5}$).

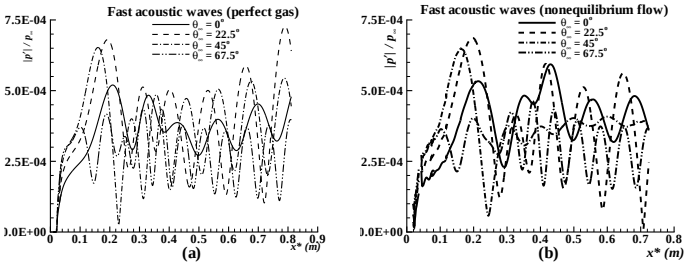

Figure 25: Distributions of pressure perturbations on the wall due to freestream plane fast acoustic waves at different incident angles ($M_\infty = 10.0$, $Re^*_\infty = 6.6 \times 10^6/m$, and $F = 5.0 \times 10^{-5}$).

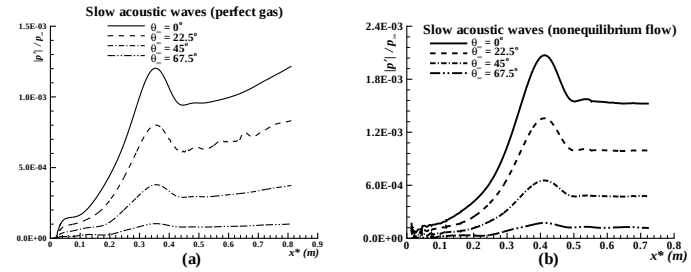

Figure 26: Distributions of pressure perturbations on the wall due to freestream plane slow acoustic waves at different incident angles ($M_\infty = 10.0$, $Re^*_\infty = 6.6 \times 10^6/m$, and $F = 5.0 \times 10^{-5}$).

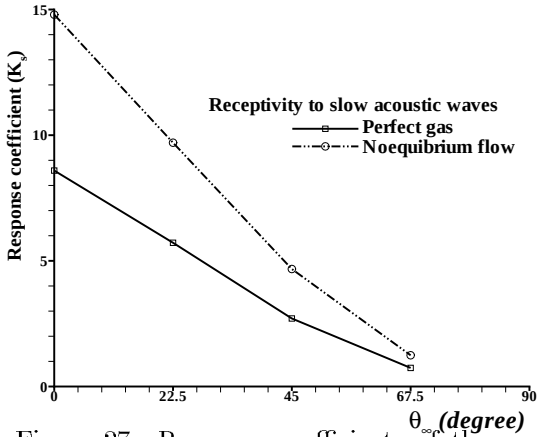

Figure 27: Response coefficients of the second mode to freestream acoustic waves vs. incident wave angles ($M_\infty = 10.0$, $Re^*_\infty = 6.6 \times 10^6/m$, and $F = 5.0 \times 10^{-5}$).

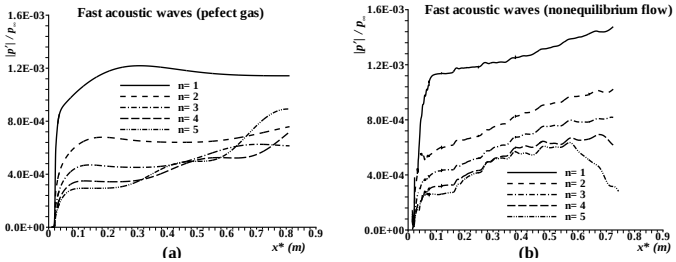

Figure 28: Comparison of presure perturbations along the wall surface due to freestream plane fast acoustic waves at different frequencies ($M_\infty = 10.0$, $\theta_\infty = 0°$ and $Re^*_\infty = 6.6 \times 10^6/m$).

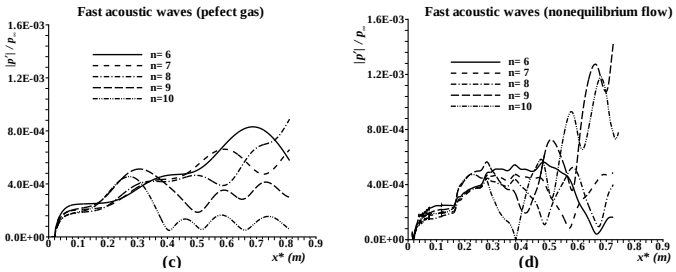

Figure 29: Comparison of presure perturbations along the wall surface due to freestream plane fast acoustic waves at different frequencies ($M_\infty = 10.0$, $\theta_\infty = 0°$ and $Re^*_\infty = 6.6 \times 10^6/m$).

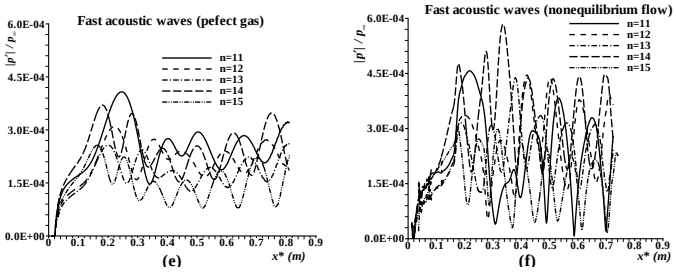

Figure 30: Comparison of presure perturbations along the wall surface due to freestream plane fast acoustic waves at different frequencies ($M_\infty = 10.0$, $\theta_\infty = 0°$ and $Re^*_\infty = 6.6 \times 10^6/m$).

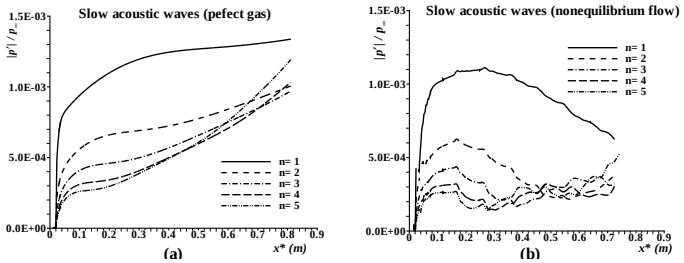

Figure 31: Comparison of presure perturbations along the wall surface due to freestream plane slow acoustic waves at different frequencies ($M_\infty = 10.0$, $\theta_\infty = 0°$ $Re^*_\infty = 6.6 \times 10^6/m$).

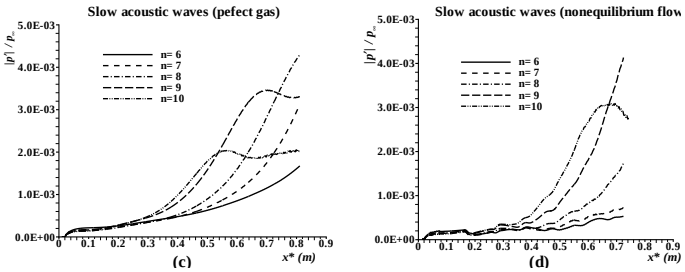

Figure 32: Comparison of presure perturbations along the wall surface due to freestream plane slow acoustic waves at different frequencies ($M_\infty = 10.0$, $\theta_\infty = 0°$ and $Re^*_\infty = 6.6 \times 10^6/m$).

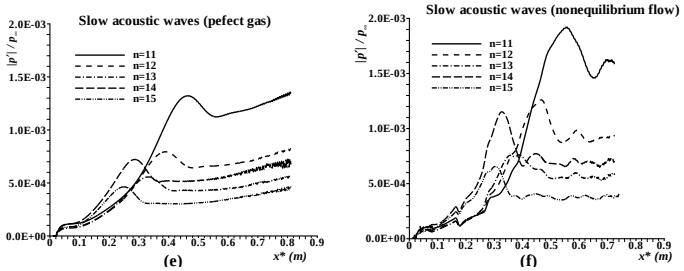

Figure 33: Comparison of presure perturbations along the wall surface due to freestream plane slow acoustic waves at different frequencies ($M_\infty = 10.0$, $\theta_\infty = 0°$ and $Re^*_\infty = 6.6 \times 10^6/m$).

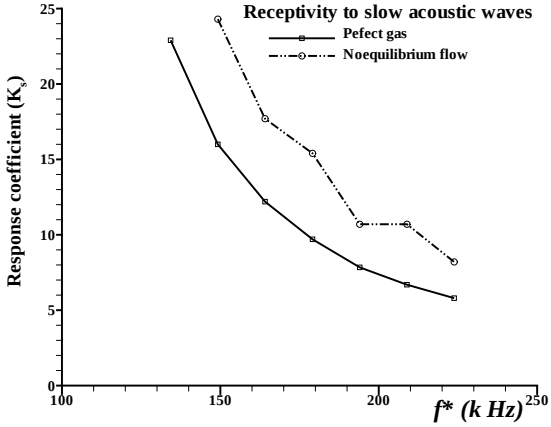

Figure 34: Response coefficients of the second mode to freestream slow acoustic waves at different frequencies ($M_\infty = 10.0$, $Re^*_\infty = 6.6 \times 10^6/m$ and $\theta_\infty = 0°$